

Quantum reservoir computing in atomic lattices

Guillem Llodrà,^{1,*} Pere Mujal,² Roberta Zambrini,¹ and Gian Luca Giorgi^{1,†}

¹*Institute for Cross-Disciplinary Physics and Complex Systems (IFISC) UIB-CSIC,
Campus Universitat Illes Balears, Palma de Mallorca, Spain.*

²*ICFO-Institut de Ciències Fotoniques, The Barcelona Institute of
Science and Technology, 08860 Castelldefels (Barcelona), Spain*

(Dated: November 21, 2024)

Quantum reservoir computing (QRC) exploits the dynamical properties of quantum systems to perform machine learning tasks. We demonstrate that optimal performance in QRC can be achieved without relying on disordered systems. Systems with all-to-all topologies and random couplings are generally considered to minimize redundancies and enhance performance. In contrast, our work investigates the one-dimensional Bose-Hubbard model with homogeneous couplings, where a chaotic phase arises from the interplay between coupling and interaction terms. Interestingly, we find that performance in different tasks can be enhanced either in the chaotic regime or in the weak interaction limit. Our findings challenge conventional design principles and indicate the potential for simpler and more efficient QRC implementations tailored to specific tasks in Bose-Hubbard lattices.

I. INTRODUCTION

Despite significant progress in quantum computing, the quest for large-scale, fault-tolerant, and universal implementations suited for practical problems remains an ongoing challenge [1–3]. The current noisy intermediate-scale quantum (NISQ) devices [4, 5], characterized by a small number of quantum units and moderately high error rates, are not yet capable of achieving the practical purposes of the pioneering and promising algorithms [6, 7] that boosted the development of current conventional gate-based technologies in qubit systems. NISQ devices fostered advances in machine learning (ML), mainly in variational quantum algorithms (VQA) [8]. Nevertheless, the training process of these parameterized circuits presents significant challenges that limit their successful implementation, as evidenced by the phenomenon of barren plateaus [9, 10].

Together with the advancement of quantum computing, quantum simulators have emerged, inspired by Feynman’s concept of emulating the behavior of a quantum system of interest by utilizing an equivalent one [11]. The notable progress obtained in the control and manipulation of quantum systems, coupled with a significant reduction in hardware requirements, has resulted in the development of quantum simulators. Currently, these are predominantly implemented in analog systems [12–14], although proposals for digital gate-based ones also exist [15]. In particular, one successful approach to quantum simulation is the use of Bose-Einstein condensates (BECs) [16, 17]. By exploiting the unique properties of BECs, a wide range of quantum phenomena have been simulated, from superfluidity [18–21] and superconductivity [22, 23], to quantum phase transitions and many-body localization [24, 25], and topological gauge theories

[26]. Additionally, cold atom experiments with quantum gas microscopes have reached an unprecedented control over the preparation, manipulation and read-out of highly isolated systems of large ensembles of both bosonic and fermionic atomic species [27–32].

A less explored avenue for these quantum simulators is in the context of unconventional and neuromorphic computing [33–35], where these platforms can be adapted and exploited to implement novel algorithms and protocols. One promising application, inspired by recurrent neural network, at the intersection of unconventional computing, machine learning, and analog systems, is quantum reservoir computing (QRC) [35, 36]. Reservoir computing is a supervised machine-learning technique allowing for in-memory processing and easy training, where the reservoir is kept fixed and only the output layer is trained, usually using a simple linear regression, that allows for efficient training and multitasking [37–39]. Beyond inheriting the advantages of classical settings, QRC approach targets either classical or quantum temporal information processing, enhanced by the large state dimension and capabilities of quantum physical reservoirs, even in NISQ devices [35].

The performance of QRC depends on the echo state and fading memory [40–44] properties, as well as a suitable nonlinear input-output transformation [45, 46], associated to the proper hyperparameters choice [47]. The potential of QRC has been demonstrated through their information processing capacity [48] and other memory tasks [36, 49], and in forecasting, as dynamical system [50] chaotic [51] or financial [52–54] time series predictions. Examples of static tasks, that can be realized also in absence of internal memory –a setting known as Quantum Extreme Learning Machine (QELM)– are entanglement detection [55] or ground-state finding [56] among others [35]. Experimental realizations of QRC and QELM have already been reported in nuclear magnetic resonance [57], superconducting qubits [58–62], photonic setups [63], and Rydberg atoms [64, 65].

In this work, we consider a one-dimensional Bose-

* guillemllodra@ifisc.uib-csic.es

† gianluca@ifisc.uib-csic.es

Hubbard model as a quantum reservoir, focusing on two key questions: optimizing the operational regime and understanding the role of disorder, often considered an essential ingredient for QRC. To address these, we numerically investigate the dynamics of the Bose-Hubbard model for different QRC benchmarking tasks in the crossover between superfluid and Mott-insulator phase [66], experimentally tested in [67–70]. Recently, it was shown that signatures of quantum chaos arise in a transition regime in the Bose-Hubbard model [71, 72]. Following the results reported in [48], we aim to address the relative performance of QRC in this quantum chaos regime with respect to the limits where interactions or hopping dominate.

We also address the role played by disorder and symmetries in QRC substrates. While simple periodic structures like one-dimensional chains exhibit limited performance, breaking translational symmetry in (classical and quantum) reservoirs is known to significantly enhance processing performance [73–75]. Actually, with the exception of (problem related) symmetries that can prove beneficial [76], generic tasks lack known symmetries and these are detrimental [47, 77, 78]. In our study, we show that QRC can be implemented using more straightforward configurations not requiring to tune the Bose-Hubbard lattice towards inhomogeneous configurations, which may facilitate the conduct of practical experiments with actual quantum devices.

The paper is organized as follows. We first introduce the Bose-Hubbard model and discuss its phases and quantum chaos in section II. Section III contains all the details about the quantum reservoir computing algorithm. Then, in section IV there is an analysis on the performance depending on the dynamical regime for different benchmarking tasks. Section V addresses the impact of finite measurements on the previous tasks. In section VI, we focus on the performance across different topologies, highlighting their influence on learning capabilities. Finally, the conclusions are presented in section VII.

II. BOSE-HUBBARD MODEL

We consider a one-dimensional chain of interacting bosons as a quantum reservoir computer, described by the Bose-Hubbard Hamiltonian [17, 66, 79, 80]:

$$H = -J \sum_{j=1}^N (b_j^\dagger b_{j+1} + \text{h.c.}) + \frac{U}{2} \sum_{j=1}^N n_j (n_j - 1), \quad (1)$$

where $b_j^\dagger (b_j)$ are the bosonic creation (annihilation) operators at site j , n_j is the number operator, J is the tunneling parameter characterizing the boson mobility between nearest-neighbor sites, and U is the on-site repulsive ($U > 0$) interaction strength. The Bose-Hubbard model has three important symmetries: \mathbb{Z}_2 , translational –under periodic boundary conditions– and conservation

of the total boson occupation number. While these symmetries simplify the model, we anticipate that they can be detrimental to fully exploiting the capabilities of quantum reservoir computing limiting its expressivity (see Section VI). In this work, we consider mainly a chain with open boundaries (where $b_{N+1} = 0$), but also periodic boundaries (where $b_{N+1} = b_1$), the disordered chain with inhomogeneous (and random) tunneling couplings ($J \rightarrow J_{j,j+1}$), and all-to-all network.

The interplay between the Hamiltonian terms leads to a rich variety of regimes [17, 67–69, 81–83]. In the limit of strong on-site interaction ($U \gg J$), the ground state of the system is in the Mott-Insulator (MI) phase [17, 67], where each site is occupied by a fixed number of bosons, and the tunneling between sites is suppressed. In the opposite limit, ($U \ll J$) the ground state of the system is in the superfluid (SF) phase [17, 67], where the bosons can move freely through the chain. Recently, looking at the full energy spectrum of the Hamiltonian in the region where $U \sim J$, signatures of a dynamical phase transition to chaos were reported [71, 84]. It was shown that the distribution of energy level spacings follows a Wigner-Dyson distribution [85]. In the following, we will mainly be concerned with the dynamical phases of the system, which are candidates to play a determinant role in the reservoir capabilities [47]. With abuse of language by mixing nomenclatures from quantum phase transitions and dynamical phase transitions, and for the sake of simplicity, we will refer to the different parameter regions as the MI phase ($U \gg J$), the chaotic phase ($U \sim J$) and the SF phase ($U \ll J$).

Among tools to identify the presence of quantum chaos, random matrix theory (RMT) (originated from understanding energy level statistics in complex nuclei [86]) has become a fundamental framework in the analysis of quantum many-body spectra [87]. Let us consider the distribution of level spacing, $p(s)$, between consecutive energy levels, $s_n = E_{n+1} - E_n$. According to RMT, when $p(s)$ follows a Poisson distribution, the system tends to be integrable, while a Wigner-Dyson distribution signifies chaotic behavior. Different underlying symmetries of the system correspond to different ensembles of random matrices, with the Gaussian orthogonal ensemble (GOE) being particularly pertinent for studying systems like the Bose-Hubbard model [71, 72]. Furthermore, methods like the gap ratio, $r_n = \min(s_n/s_{n-1}, s_{n-1}/s_n)$, introduced by Oganessian and Huse [85] simplify the calculations and gave a clear indicator of ergodicity, $\langle r \rangle_{GOE} \approx 0.5359$, and integrability, $\langle r \rangle_{\text{Poisson}} \approx 0.3863$ [88, 89]. This indicator was used in Refs. [47, 90] as a marker of the QRC regimes and related capabilities for the transverse Ising model.

The transition to chaos in the Bose-Hubbard model has recently been analyzed by Pausch *et al.* [71, 72]. In these works, the authors examined the eigenvalue spacing, as characterized by $\langle r \rangle$, and the eigenstate structure, through the so-called generalized fractal dimension (GFD). These measures allow for the distinction

between localization, multifractality (extended non-ergodic), and ergodicity. Given a state $|\psi\rangle = \sum_{\alpha} \psi_{\alpha} |\alpha\rangle$ (where $\{|\alpha\rangle\}$ is a complete basis that spans a Hilbert space of dimension \mathcal{N}), among all the finite-size GFDs, we will consider the quantity \tilde{D}_1 , known as the *information dimension* [91], which determines the scaling behavior of the Shannon information entropy: $\tilde{D}_1 = -(\ln \mathcal{N})^{-1} \sum_{\alpha} |\psi_{\alpha}|^2 \ln |\psi_{\alpha}|^2$. The thermodynamic limit of this quantity, $D_1 = \lim_{\mathcal{N} \rightarrow \infty} \tilde{D}_1$ provides insight into the eigenstate distribution in the Hilbert space. For $D_1 = 1$, the state is spread uniformly over the entire Hilbert space, which is a signature of ergodicity. On the other hand, $D_1 = 0$ corresponds to a perfectly localized state. For intermediate values, $0 < D_1 < 1$ the system exhibits multifractal behavior, characterized by a complex combination of localization and ergodicity. In such cases, the wavefunction occupies a fractal subset of the Hilbert space, extending non-ergodically as discussed in [91].

The behavior of both $\langle r \rangle$ and $\langle \tilde{D}_1 \rangle$ (where the basis $\{|\alpha\rangle\}$ corresponds to the Fock basis in this context) is reproduced in Fig. 1 for Bose-Hubbard reservoirs with chain sizes from $N = 5$ to $N = 7$. One can see that multifractality is a sensitive tool for characterizing the emergence of chaos, with plateau values closely matching the GOE values, as indicated by the black lines in Fig. 1. We will see that this behavior has important consequences once we look at the QRC capabilities of the model in the different dynamical regimes.

III. QUANTUM RESERVOIR COMPUTING BASED ON THE BOSE-HUBBARD MODEL

Let's briefly introduce the machine learning approach of QRC that will be realized with a Bose-Hubbard chain substrate. This is composed of three fundamental layers, as illustrated in Fig. 2. A (classical or quantum) input signal is fed into the reservoir. In this case, a one-dimensional chain of atoms processes the received information. Then, meaningful features from the reservoir are extracted at the output layer as a set of observables. Suppose our input consists of a sequence of values $\{s_1, s_2, \dots, s_k, \dots\}$ drawn independently from a uniform distribution within the interval $[0, 1]$. At every time step k , an input value is injected into one of the nodes of the bosonic chain by resetting one atom state (let us choose site 1 for the sake of convenience)

$$|\psi_k\rangle = \sqrt{s_k} |0\rangle + \sqrt{1 - s_k} |1\rangle. \quad (2)$$

Once, the input s_k has been encoded, the reservoir evolves under the unitary evolution associated with the Hamiltonian in Eq. (1). The sequence of input injection and Hamiltonian evolution describes a completely positive trace preserving (CPTP) map of the form

$$\rho_k = e^{-iH\Delta t} [\rho_{1,k} \otimes \text{Tr}_1 \{\rho_{k-1}\}] e^{iH\Delta t}, \quad (3)$$

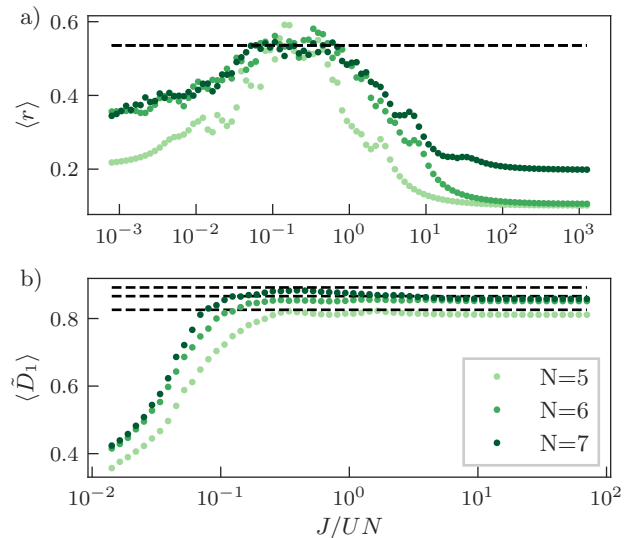


FIG. 1. (a) Distribution of the average level spacing ratios $\langle r \rangle$ over the inner 70% of the eigenenergies as a function of J/UN for one-dimensional open with parity ($\pi = -1$) at unit-filling ($N = N_e$) being N (N_e) the number of sites (excitations) in the chain. (b) Evolution of $\langle \tilde{D}_1 \rangle$ as a function of J/UN . The data is averaged from the amplitudes ψ_{α} of the 100 eigenvectors closest to rescaled energy, $\epsilon = (E - E_{min}) / (E_{max} - E_{min}) = 0.5$ where α represents the Fock basis. The black line corresponds to the expected results for $\langle r \rangle_{GOE} \approx 0.5359$ and $\langle \tilde{D}_1 \rangle = (H_{N/2} - 2 + \ln 4)(\ln \mathcal{N})^{-1}$ [71] being $\mathcal{N} = 60, 226, 848$ for $N = 5, 6, 7$, respectively.

where $\text{Tr}_1 \{\cdot\}$ denotes the partial trace performed over the first site and $\rho_{1,k} = |\psi_k\rangle\langle\psi_k|$. It is important to notice that time step Δt controls the amount of time the information from value s_k propagates through the system. Finally, the output layer consists of measuring a set of M observables (O_i) from the quantum reservoir to extract M features, $\{x_i^{(k)}\}_{i=1}^M$, defined as

$$x_i^{(k)} = \text{Tr} [O_i \rho_k]. \quad (4)$$

This erase-and-write scheme is based on the original proposal of Fujii and Nakajima (for spins) in Ref. [36] and produces a nonlinear input-output mapping where the encoding plays a key role, as discussed in more detail in Ref. [43, 45]. The reservoir retains information about past inputs, allowing it to maintain a memory of different input patterns, which is a crucial aspect of QRC that distinguishes it from other approaches like Quantum Extreme Learning Machines. This memory capability is essential for online processing of time-dependent data.

A comprehensive training dataset, denoted as X , can be constructed by combining all the features, $x_i^{(k)}$, with dimensions $L \times (M + 1)$. Here, L represents the number of training inputs (s_k), while $M + 1$ accounts for the number of observables plus a constant bias term. In the tasks analyzed in the following we will consider an out-

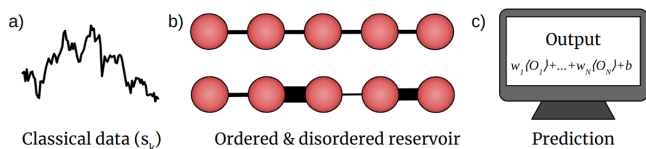


FIG. 2. Illustration of the Quantum Reservoir Computing algorithm steps. a) Classical data ($s_k = [0, 1]$) is fed into the first site of the system. b) The classical data is processed through a one-dimensional quantum reservoir. In this work, we will compare the performance of a homogeneous and heterogeneous system. c) Output predictions are generated based on the expected values of the quantum system.

put layer consisting of two sets of observables $\langle a_i^\dagger a_j + h.c. \rangle$ and $\langle a_i^\dagger a_i a_j^\dagger a_j \rangle$ for all sites. Additional features can be extracted from the dynamics by leveraging the temporal multiplexing technique [36]. Specifically, instead of measuring an observable at time Δt , the unitary evolution can be divided into V time intervals. This enables a larger dataset with dimensions $L \times (VM + 1)$, where V is the number of virtual nodes [48]. Unless otherwise stated, in all results presented, a total of $V = 10$ virtual nodes are employed.

The learning stage consists of three phases: wash-out, training, and testing, of different lengths. In the wash-out step, we evolve the system during a transient of 100 time steps, in order to mitigate the influence of initial conditions on the system's performance, thereby ensuring the fulfillment of the echo state property [40, 92]. Subsequently, a linear regression model

$$y_k = \sum_i w_i x_i^{(k)} + b_k, \quad (5)$$

is trained during $L = 1000$ time steps. Here w_i and b_k are optimized to minimize a Ridge regression loss function with a regularization parameter of $\beta = 10^{-2}$ [93, 94]. It is crucial to note that parameters in the reservoir are fixed and only the output layer parameters are optimized during this step. Finally, the system is tested in 1000 time steps, making predictions in different tasks \hat{y}_k and evaluating the model's performance (i.e. the ability of y_k to approximate \hat{y}_k for unseen inputs) with the optimized parameters. In Sec. IV we will present results for different tasks, considering expectation values on an infinite number of reservoirs, while in Sec. V we analyze the performance beyond ideal conditions, with a finite ensemble of identical reservoirs, leading to statistical errors in the measured quantities at the output layer [95, 96].

A. Reservoir in different regimes

Before addressing specific tasks, let us consider the limiting regimes of the Bose-Hubbard reservoir. With respect to previous works of bosonic QRC in harmonic networks [43, 49, 97, 98], a Bose-Hubbard reservoir displays interactions, that can expand the capabilities of

QRC beyond Gaussian states for machine learning purposes (as started to be explored in QRC [99] and other variational settings [100]). However, the interplay with many-body effects also plays a key role. We advance that we find (see section IV) that in the presence of very strong interactions, the QRC performance is actually hindered in the present setting. In the limit case $J \ll U$, when the interaction term completely dominates, Eq. (1) is approximated by $H_I = \frac{U}{2} \sum_{j=1}^N n_j(n_j - 1)$, and the ground state exhibits the Mott-Insulator phase. Then, the dynamics of each node in the network becomes decoupled from the others and the locally encoded information does not propagate through the system. Consequently, the information injected at iteration k into the first node in Eq. (3) is completely erased at the next time step, $k + 1$. Therefore, the system has no memory and is unable to perform temporal tasks. This regime extends also for finite, yet small values of J/U , where the system still exhibits localization, which has been reported to be a hindering factor for QRC [47, 101].

In the limit case $J \gg U$, the system becomes a Bose-Einstein condensate, described by the coupling term $H_C = -J \sum_{j=1}^N (b_j^\dagger b_{j+1} + h.c.)$. In this superfluid regime, information encoded into the first node rapidly propagates to the other nodes. This can be seen for the homogeneous open chain by diagonalizing H_C using the Fourier transformation, which yields a ground state $|\psi\rangle_C \propto (\sum_{j=1}^N b_j^\dagger)^{N_e} |0\rangle$, where N_e are the number of excitations over the entire lattice [17, 67]. In this regime, the eigenstates are delocalized in real space, facilitating the propagation of information across the network. The delocalization feature ensures that local erasure of information does not hinder information storage (that can be present globally), so the system maintains memory of the inputs over time, making the QRC algorithm effective. Furthermore, the reservoir operation for a complex bosonic network, in the case of $U = 0$ and a fully connected random network has already been reported to operate as a QRC [92].

Thermalized quantum reservoirs near the phase transition boundary have been found to excel in nonlinear learning tasks, for disordered spin systems [47, 101]. In contrast, our study reveals that a one-dimensional bosonic reservoir can also enhance learning capabilities near the phase transition, without requiring disorder. Furthermore, we establish a direct link between performance and the underlying physics of the Hamiltonian demonstrated by the $\langle r \rangle$ metric (Fig. 1a) and more notably by the $\langle \tilde{D}_1 \rangle$ metric (Fig. 1b) [71, 72, 84], still unexplored in the context of QRC. Most work on QRC considers disordered reservoirs, which are expected to increase the expressivity of the system. In contrast, regular lattices exhibit symmetries that may reduce the linear independence of the output layer features. However, our conjecture is that the dynamical phase sets the capability of the system to process information being disorder less relevant, at least in small reservoirs.

In the following, we will address different QRC tasks considering the Bose-Hubbard reservoir for different relative strengths of interaction and tunneling and selecting three representative regimes for the Mott-Insulator ($J/U = 10^{-3}$), chaotic ($J/U = 0.1$), and superfluid ($J/U = 10^3$) regimes. We will then compare different topologies, such as periodic, open, and disordered atomic chains.

IV. RESERVOIR PERFORMANCE

In this section, we assess the capabilities of a one-dimensional reservoir, either homogeneous or not, with open boundary conditions through a series of benchmarking tasks, including Short-Term Memory (STM), Parity Check (PC), and the Nonlinear AutoRegressive Moving Average (NARMA). These tasks serve as common indicators for evaluating two ingredient components to process temporal information: memory and nonlinearity.

A. Short-Term Memory task

The first task consists of evaluating the memory capacity through the STM task, which displays the system's ability to retain information from previously injected inputs. Specifically, an input s_k is injected into the system at each step k and the target is the previous one for a given delays (τ)

$$\hat{y}_k = s_{k-\tau}. \quad (6)$$

Ultimately, the memory capacity is evaluated through a correlation, specifically the square of the Pearson factor, between the output, represented by y_k , and the target \hat{y}_k :

$$C = \frac{\text{Cov}^2(\hat{y}_k, y_k)}{\sigma^2(y_k)\sigma^2(\hat{y}_k)}, \quad (7)$$

where $\sigma(\cdot)$ is the standard deviation and $\text{Cov}(\cdot)$ indicates the covariance. The metric C is constrained between $C = 0$ (no ability to recall past inputs) and $C = 1$ (perfect recall of past inputs).

Let us start our analysis by looking at the solid lines in Fig. 3a. Here, we analyze how memory capacity decays as we increase the delay across different dynamical phases: Mott-Insulator (green), quantum chaos (red), and superfluidity (blue). To simulate the dynamics numerically, we apply a cut-off of $n_c = 3$ on each site, which is sufficient to accurately describe the exact evolution of the system, as shown in Appendix B. As expected from the discussion in Sec. III A, the system lacks memory in the Mott-Insulator phase because injected information does not spread and is wiped out in the next time step. For $\tau = 0$ the memory capacity is maximum ($C = 1$), but as soon as a new signal s_{k+1} is introduced, the memory capacity drops to $C = 0$ for $\tau \geq 1$ (green line in Fig. 3a).

As J/U increases, the system becomes better at recalling previous inputs for longer times, achieving a memory capacity of $C \geq 0.8$ at $\tau = 9$ ($\tau = 6$) in the quantum chaos (superfluidity) regime.

In particular, for $J/U = 0.1$ (red line in Fig. 3a) the system shows better memory capacity than for $J/U = 10^3$ (blue line). To clarify whether the quantum chaotic regime has an advantage over the superfluidity regime in terms of memory capacity, Fig. 3b plots the maximum delay (τ) with an STM capacity (C) greater than 0.8 for different values of J (star-marked points). Fig. 3b shows a peak in memory capability within the quantum chaotic regime relative to the superfluidity regime. For each value of J we have tuned the time step $\Delta t \in [1, 10]$ to achieve the best possible results.

In Fig. 3b we also compare the case of a homogeneous chain (solid line) with the case of a heterogeneous one (dashed line), which shows comparable performance. For the heterogeneous chain, we have introduced disorder in the coupling term (see Eq. (1)). Namely, each coupling term is defined as $J_{j,j+1} \in [J_{min}, J_{max}]$ drawn from a random uniform distribution where $J_{min} = J(1 - \delta)$ and $J_{max} = J(1 + \delta)$. We have considered a disorder level of $\delta = 0.3$ and averaged the results over 10 realizations to ensure statistical significance. Looking at both, the STM capacity at different delays and the performance across regimes, disorder does not play a significant role, with heterogeneous chains displaying even less capacity than homogeneous ones.

Let us now study the ability of our system to remember a nonlinear function of an input s_k , so the target function is defined as

$$\hat{y}_k = s_{k-\tau}^d \quad (8)$$

where d represents the degree of the nonlinearity of the input. Fig. 4 presents a comparative analysis between the linear and the nonlinear case (cubic, $d = 3$) by elucidating how distinct dynamical regimes recall nonlinear input functions. In general, we find that the memory capacity decreases with the nonlinearity. Notably, disparities emerge in the performance decay between the superfluidity and quantum chaos regimes. In the superfluidity regime (blue), the memory capacity remains close to one for low delays before exhibiting a pronounced decay with higher delays. Conversely, in the chaotic regime (red), the memory capacity slightly drops at first, especially if we compare the difference between $d = 1$ and $d = 3$ but for large delays, it clearly outperforms the superfluidity regime for a linear ($d = 1$) and a nonlinear ($d = 3$) task. Once again, in the Mott-Insulator regime, there is no memory capacity for $\tau \geq 1$.

B. Parity Check task

The model's ability to process highly nonlinear information is displayed considering the Parity-Check (PC) task. For this task, we inject a binary random input

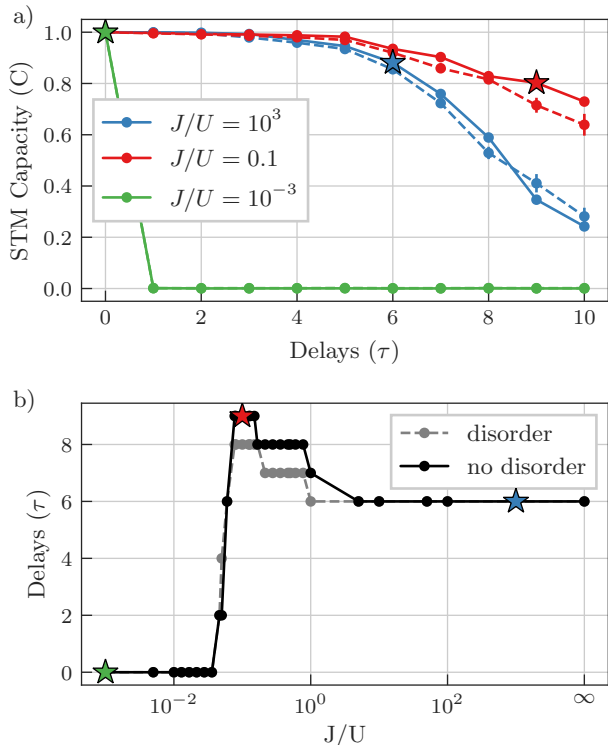


FIG. 3. Performance analysis of the short-term memory task changing the coupling strength. (a) Memory capacity as a function of the input delay for dynamical regimes: Mott-Insulator (green), quantum chaos (red), superfluidity (blue). (b) Maximum delay achieved with a memory capacity above 0.8. The solid (dashed) line represents a homogeneous (heterogeneous with disorder $\delta = 0.3$) open-chain of $N = 5$ sites with a cut-off $n_c = 3$. The reservoir system is trained and tested with 1000 time steps after a wash-out time of 100 (500) time steps if $J/U \geq 0.1$ ($J/U < 0.1$). The evolution time ($\Delta t \in [1, 10]$) has been optimized to achieve the best performance. The output layer consists of two sets of observables $\langle a_i^\dagger a_j + h.c. \rangle$ and $\langle a_i^\dagger a_i a_j^\dagger a_j \rangle$, number of virtual nodes $V = 10$, ridge regression $\beta = 0.01$, initial state of the reservoir all zeros states. For the disordered system, we have averaged over 10 realizations and show the standard error of the mean as the statistical error, in most of the cases below the sign of the symbol.

($s_k \in \{0, 1\}$) and train the system to fit the following target function

$$\hat{y}_k = \sum_j^\tau s_{k-j} \pmod{2}. \quad (9)$$

Looking at Fig. 5, we can see that the outcome of the parity check task differs notably from the short-term memory task (Fig. 3). In Fig. 5a, the performance of the quantum chaos regime drops quickly, but the superfluidity regime maintains a PC capacity above 0.8 for longer delays. Exploring all regimes there is no peak in Fig. 5 unlike in the STM task (Fig. 3), where performance has

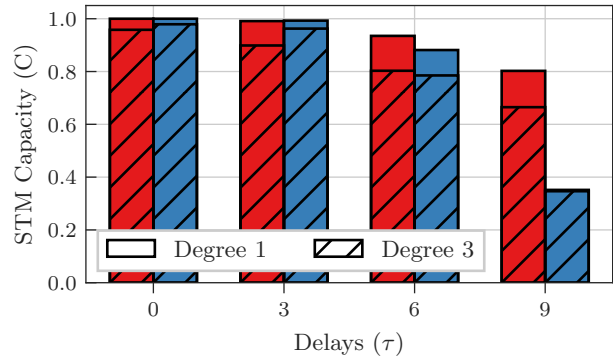


FIG. 4. Linear and nonlinear memory capacity as a function of the delay with degrees $d = 1$ and $d = 3$. The optimal evolution time for the quantum chaos regime (red) is $\Delta t = 10$, while for the superfluidity regime (blue) it is $\Delta t = 1$. All other parameters remain consistent with those in Fig. 3. At $\tau = 9$ both performances reach $C = 0.35$ after rounding up the third decimal point.

a maximum near the transition. The lack of such a peak for the parity check is also observed in Xia *et al.* [101] (check their Fig. 3) and in Martínez-Peña *et al.* [47] (Fig. 9) for the nonlinear memory indicator known as information processing capacity [102]. This is also foreseen from our Fig. 4, as increasing the degree of nonlinearity reveals that memory capacity is superior in the superfluidity regime compared to the transition phase, at least for low delays. Interesting, the behavior of the memory capacity for this task, in Fig. 5b, looks very similar to the information dimension shown in Fig. 1. This seems to indicate that, besides the chaotic regime, efficient QRC is highly related to the eigenvector spreading over the lattice, also in the presence of conserved quantities. Finally, in this task, we can also observe that the performance of a homogeneous and heterogeneous chain is similar.

C. NARMA task

The NARMA task is well-suited to assess memory and nonlinearity as it simulates a nonlinear dynamical system with a strong dependence on previous inputs (s_k). Initially introduced by Atiya *et al.* [103], the NARMA(n) task, for $n > 2$, is defined as

$$\hat{y}_k = 0.3y_{k-1} + 0.05y_{k-1} \sum_{j=1}^n y_{k-j} + 1.5s_{k-n}s_{k-1} + 0.1, \quad (10)$$

where s_k is the input, \hat{y}_k is the target, and n is the maximum delay. On the other hand, the NARMA(2) task reads

$$\hat{y}_k = 0.4y_{k-1} + 0.4y_{k-1}y_{k-2} + 0.6s_{k-1}^3 + 0.1, \quad (11)$$

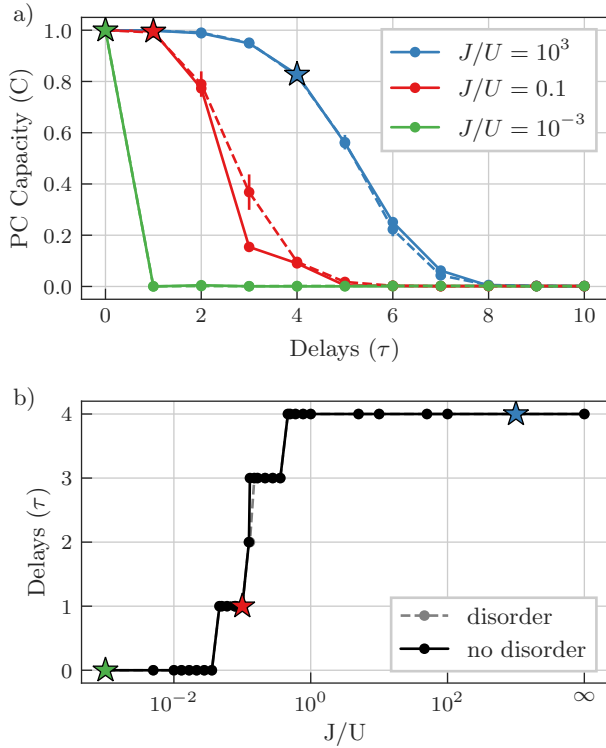


FIG. 5. Performance analysis of the parity check task. (a) Memory capacity as a function of the delay for a homogeneous (solid) and inhomogeneous (dotted) one-dimensional chain with open-boundary conditions. (b) Performance for different values of J/U during the transition Mott-Superfluidity, signaling the maximum delay achieved with memory capacity above 0.8. All remaining parameters are consistent with those in Fig. 3.

For this task, the input s_k is generated from a random uniform distribution ranging from 0 to 0.2 as in Ref. [36]. To solve the task, the reservoir computer needs to replicate a quadratic nonlinear function of the input sequence up to the maximum delay n , see Eq. (10) for $n > 2$ and Eq. (11) for $n = 2$.

In Fig. 6, we plot the performance achieved for different NARMA tasks ranging from NARMA(2) to NARMA(14) and for different values of J/U . To quantify the capability of the system we set three threshold capacities $C \geq 0.7$ (light grey), $C \geq 0.8$ (grey), and $C \geq 0.9$ (dark grey) to examine how the memory capacity decays as the order of the nonlinearity (n) increases. In the Mott-Insulator phase, the capacity never surpasses $C \geq 0.7$. Then, as the system transitions into the quantum chaos phase, a sudden peak is observed, with NARMA(14) exhibiting a memory capacity above 0.7. This peak is gradually reduced, with the system only reaching the $C \geq 0.8$ and $C \geq 0.9$ thresholds for NARMA(11) and NARMA(6). Notably, as the system enters the superfluidity regime, the capacity for the three thresholds reaches a plateau, indicating a decline com-

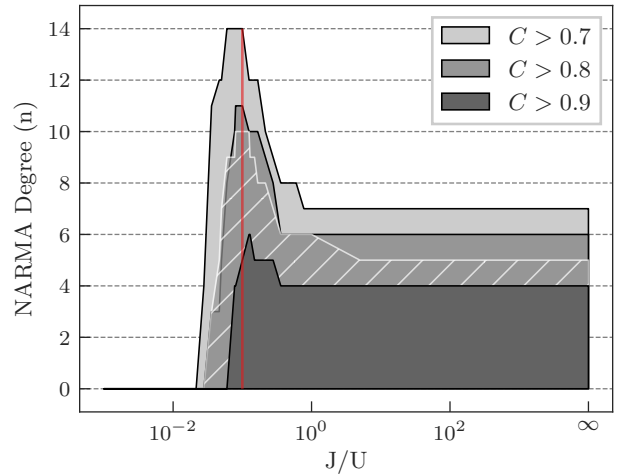


FIG. 6. Performance analysis of the NARMA task. Memory capacity (greyscale) as a function of NARMA (y -axis) and the coupling strength (x -axis). In the quantum chaos phase, there is a notable peak for NARMA(14) with $C \geq 0.7$ and NARMA(5) with $C \geq 0.9$ at $J = 0.1$, highlighted by the red line. A. White lines overlapping the $C \geq 0.8$ region represent the averaged results of a heterogeneous chain with disorder ($D = 0.3$) over 10 realizations. All remaining parameters are consistent with those in Fig. 3.

pared to the transition regime in the system's ability to retain memory as the task complexity increases.

In Fig. 6, we also analyze the effects of disorder. To avoid redundancy, we only present the results for the disordered chain in the case of a performance threshold $C \geq 0.8$. As with the previously discussed tasks, there is no significant difference between using disorder (white) and no disorder (grey), as the memory profile follows a similar pattern across all regimes.

To summarize our main results of different tasks, let us focus on Fig. 7. First, the performance can reach its peak in the quantum chaotic or the superfluid regime, depending on the specific task. While the quantum chaotic regime often provides the highest performance, as indicated by the bar height consistently matching or exceeding the blue line (representing the superfluidity phase), there are cases where the superfluid regime outperforms the chaotic regime. Secondly, for a one-dimensional open topology, the introduction of disorder in the coupling strength does not significantly enhance performance. Notice that the black bar (no disorder) is always equal to or higher than the grey bar (disorder). Our hypothesis is that disorder can confer advantages to systems with high symmetry, such as one-dimensional periodic systems. However, even with disorder, a one-dimensional periodic system can not surpass the capacity of a homogeneous one-dimensional open system. For further details, we direct the interested reader to section VI.

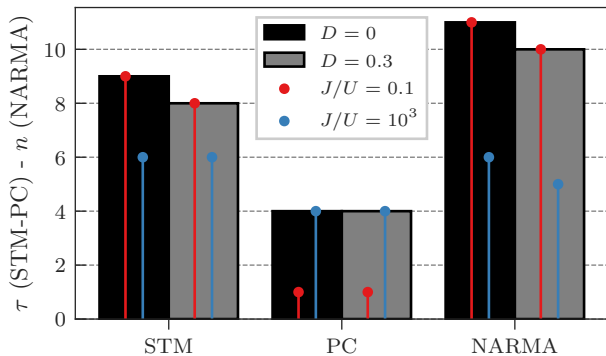


FIG. 7. Performance overview of all tasks. The bar height indicates the delay (for STM and PC tasks) and n -order (for the NARMA), with a memory capacity above 0.8. The best performance (maximum delay or order) is displayed, considering all regimes. The blue line represents the maximum capacity in the superfluidity phase while the red one is for the chaotic phase. Performance for both homogeneous (black bars) and disordered (grey bars) chains are displayed.

V. MEASUREMENTS EFFECTS

This section discusses the limits imposed by statistical noise on the previous benchmarking tasks. Concretely, we compare the performance of the STM under a finite number of measurements (N_m) and the ideal case ($N_m \rightarrow \infty$) in Sec. IV. In real experiments, the ideal expected value of any observables ($x_i^{(k)}$) is affected by the stochastic nature of quantum mechanics, which causes the appearance of statistical errors (ξ_{N_m}) that result in an experimental expected value ($x_{i,exp}^{(k)}$) deviating from the ideal $x_i^{(k)}$ leading to:

$$x_{i,exp}^{(k)} = x_i^{(k)} + \xi_{N_m}. \quad (12)$$

To simulate such a stochastic effect, numerically, we add random noise (ξ_{N_m}) drawn from a Gaussian distribution with mean $\mu = 0$ and standard deviation $\sigma = \frac{1}{\sqrt{N_m}}$. According to the central limit theorem, we expect that for $N_m \gg 1$, the experimentally measured value will converge to the ideal expected one (corresponding to an infinite ensemble) [90, 95, 97].

As shown in Fig. 8, the model's capacity improves significantly with the number of measurements (N_m). Notably, the ideal performance depicted in Fig. 3 is achieved for both $J = 0.1$ and $J = 10^3$ when $N_m = 10^6$, as illustrated in Fig. 8a and Fig. 8b, respectively. To ensure consistency in our results, we have optimized the time evolution Δt within the range $[1, 10]$ and used the same parameters as in section IV.

We want to point out that the relationship between the number of measurements and performance is model-specific and can be precisely assessed only in special cases [97]. While the precision of observable expectation values

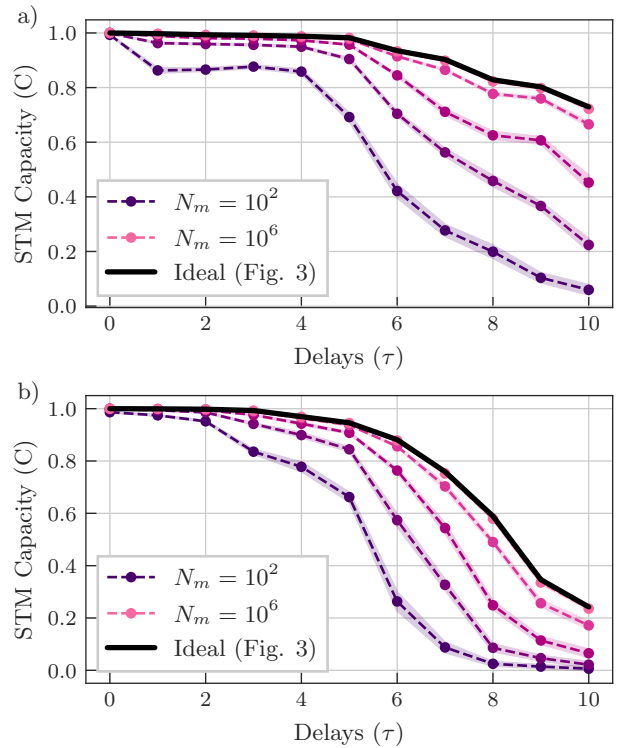


FIG. 8. Performance analysis of the STM task as a function of the delay and the number of measurements (N_m). The memory profiles show how the model's capacity improves as N_m increases for the (a) quantum chaos and the (b) superfluidity case, $J = 0.1$ and $J = 10^3$, respectively. The results are averaged over 10 realizations and the statistical error is denoted by the standard deviation.

generally improves with approximately $\frac{1}{\sqrt{N_m}}$ (see Fig. 8), translating this into performance across different tasks is complex.

VI. TOPOLOGY EFFECTS

Up to this point, we have focused on a one-dimensional chain of bosons with either homogeneous or heterogeneous coupling strengths. In this section, we extend the analysis to other topologies, beginning with a one-dimensional chain with periodic boundary conditions (PBC). In a similar spirit as in Fig. 7, in Fig. 9 we overview the three performance tasks (STM, PC, and NARMA) for a one-dimensional chain with periodic topology. Notably, Fig. 9 reveals two key findings. Firstly, comparing Fig. 7 and Fig. 9, we observe that the periodic chain generally underperforms compared to the open chain. Secondly, in contrast to the previous sections, introducing disorder can improve the model's performance. Indeed, breaking symmetries such as translational symmetry enables the model to extract novel fea-

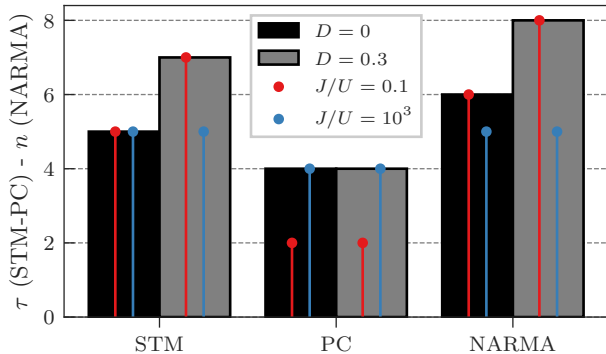


FIG. 9. Performance overview of all tasks for a one-dimensional chain with periodic boundary conditions.

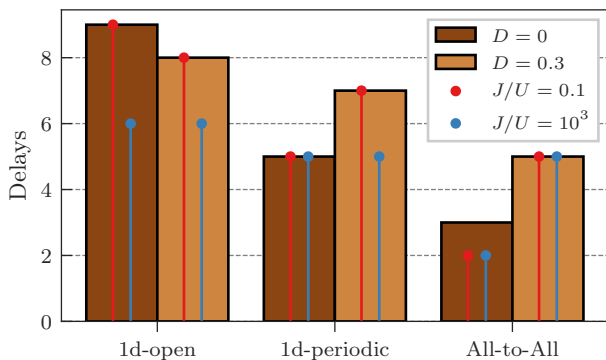


FIG. 10. Performance overview of the linear STM task for different topologies of the Bose-Hubbard model.

tures, enhancing its learning capabilities.

We now compare the performance of the various topologies in Fig. 10, also examining the all-to-all interactions, corresponding to a fully complex network. The results indicate that the one-dimensional open topology yields the best results, while the all-to-all topology performs the poorest. A deeper analysis considering the independent degrees of freedom at the output layer indicates that all-to-all network may not be well-suited for quantum reservoir computing, as the features extracted from its quantum dynamics tend to exhibit more redundancy compared to the one-dimensional open topology (see Appendix A for further details). Across all three topologies, the performance in the quantum chaos phase is either equal to or higher than that observed in the superfluidity regime, as discussed in the previous sections. Although we have chosen the STM with degree one for this analysis, the conclusions would hold similarly if the NARMA task were employed.

Intuitively, one would expect no performance difference between a periodic and open topology with disorder. However, Fig. 10 reveals that the periodic chain exhibits slightly inferior performance compared to the open

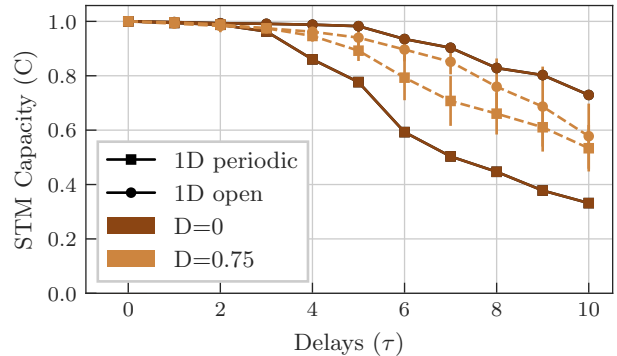


FIG. 11. Performance comparison of the linear memory capacity for different topologies. The results are averaged over 10 realizations and the statistical error is denoted by the standard deviation

chain. In Fig. 11, we observe a significant performance gap between homogeneous topologies. As the coupling disorder increases, the error bars widen, ultimately leading to similar performance for both topologies, as evident from the overlapping error bars. This result suggests that a disorder level of 0.3 is insufficient to completely erase the underlying periodic structure, allowing it to retain a weak form of translational symmetry. This residual symmetry implies that the periodic chain still preserves some level of uniformity across sites, even under moderate disorder. In fact, as disorder strength increases, the results will converge towards those of the open topology. Conversely, with very weak disorder, the periodic topology will retain its performance characteristics, similar to the case with no disorder, which explains the inferior performance in Fig. 10.

VII. CONCLUSIONS

We investigated QRC performance across three distinct dynamical regimes. First, and as expected, the Mott-Insulator phase suitability for information processing is limited, as evidenced by STM, PC, and NARMA task results. The quantum chaotic phase where the interplay of coupling and interaction is balanced is instead suited for QRC consistently with previous works [47, 101] and demonstrated superior performance in tasks demanding a balance of linear and nonlinear memory. Finally, the superfluid regime, when interactions are negligible, also yielded excellent outcomes for nonlinear tasks. This comes as a bit of a surprise, as this phase is not fully ergodic and this could be expected to limit the expressivity. By extending the results of [47], we found here that the generalized multifractal dimension is a fundamental tool to relate the QRC performance to the dynamical phases of the reservoir. Our results suggest that efficient information propagation within the system,

rather than proximity to a phase boundary, is the critical factor for QRC's success based on local input injection.

Furthermore, our topology analysis of one-dimensional chains with open and periodic boundary conditions, as well as all-to-all connectivity, revealed a surprising finding: disorder is unnecessary in systems lacking translational symmetry. The one-dimensional chain with open boundaries consistently outperformed other topologies across various benchmarks. These results challenge the conventional wisdom and suggest that more complex topologies should be explored, and prioritize OBC over PBC or all-to-all connectivity in future QRC studies. It will be interesting to test the validity of these conclusions in larger reservoirs.

To conclude, our results establish Bose-Hubbard chains as suitable QRC, not only in the chaotic phase but also in the superfluid one, and offer new insights into the design of more straightforward and efficient QRC implementations using homogeneous many-body reservoirs [104]. This work represents a promising step towards more practical experimental applications in quantum information processing, particularly for systems operating on near-term quantum devices. The results highlight the importance of selecting appropriate dynamical regimes and topologies in QRC, suggesting a path toward optimized performance without relying on complex disordered systems.

ACKNOWLEDGMENTS

We acknowledge insightful discussions during the Interantional Workshop on Disordered Systems 2024, held in Salamanca, with Andreas Buchleitner, Rafael Molina, Manuel Pino, and Alberto Rodríguez. We acknowledge the Spanish State Research Agency, through the María de Maeztu project CEX2021-001164-M funded by MCIU/AEI/10.13039/501100011033, through the COQUSY project PID2022-140506NB-C21 and -C22 funded by MCIU/AEI/10.13039/501100011033, and the QuantERA QNet project PCI2024-153410 funded by MCIU/AEI/10.13039/501100011033 and cofunded by the European Union; MINECO through the QUANTUM SPAIN project, and EU through the RTRP - NextGenerationEU within the framework of the Digital Spain 2025 Agenda. The CSIC Interdisciplinary Thematic Platform (PTI+) on Quantum Technologies in Spain (QTEP+) is also acknowledged. This project has received funding from MICIN and Generalitat de Catalunya with funding from the European Union, NextGenerationEU (PRTR-C17.I1), the Government of Spain (Severo Ochoa CEX2019-000910-S and FUNQIP), Fundació Cellex, Fundació Mir-Puig, Generalitat de Catalunya (CERCA program).

Appendix A: Singular values

As shown in Section VI, the homogeneous all-to-all topology is the least suitable for QRC due to the redundant features. In contrast, systems with no translational symmetry, such as the one-dimensional open topology, offer more promising opportunities for QRC. In this section, we will quantify the redundancy by analyzing the singular values of the training dataset (X_{train}) from Eq. (4).

In Fig. A1, we notice a striking difference in the distribution of singular values across various topologies. The all-to-all topology exhibits the largest number of singular values near zero, indicating a high degree of redundancy in the dataset. This redundancy is consistent with the poor performance observed in Fig. 10. In contrast, the one-dimensional topology exhibits a majority of non-zero singular values, suggesting that the features are less redundant and may provide better results on unseen data. This difference in redundancy highlights the importance of topology selection in achieving optimal performance.

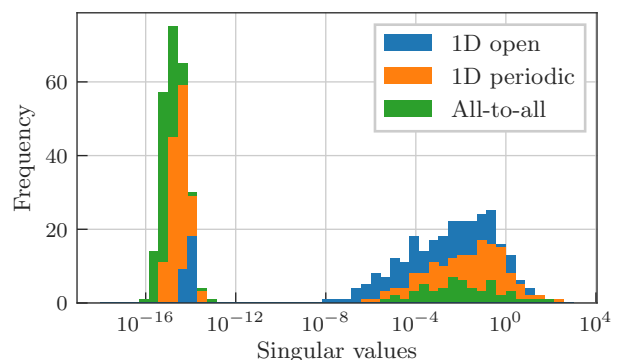


FIG. A1. Histogram with all the singular values from the X_{train} used in Fig. 10 for $D=0$.

Appendix B: Validty of numerical results

The input injection scheme utilized to implement the QRC implies a nonconservation of the number of excitations in the reservoir. Consequently, an exact simulation would require spanning the infinite-dimensional Hilbert space. However, we have checked that, in the operational regime employed, the number of excitations was always very limited. In fact, all the results presented in the main text have been obtained using a Fock-space cut-off of $n_c = 3$ for each system site. To assess the validity of this approximation, in Fig. A2 we evaluate the performance of the STM capacity for both the open and periodic chains, comparing the truncation level $n_c = 3$ with $n_c = 4$. The results demonstrate that the truncation has minimal impact on the outcome, indicating that the reservoir dynamics are accurately reproduced.

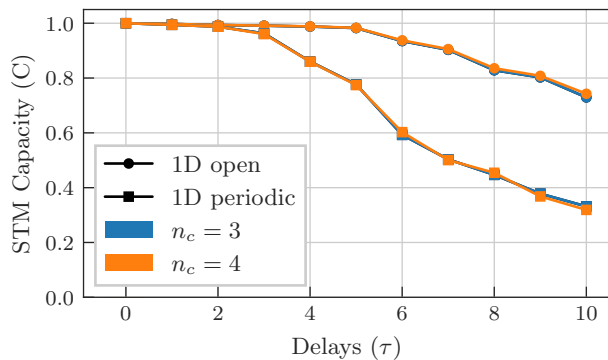


FIG. A2. Performance analysis of the STM task for different cut-off $n_c = 3$ (blue) and $n_c = 4$ (orange) for $J = 0.1$.

-
- [1] Frank Arute, Kunal Arya, Ryan Babbush, Dave Bacon, Joseph C Bardin, Rami Barends, Rupak Biswas, Sergio Boixo, Fernando GSL Brandao, David A Buell, et al. Quantum supremacy using a programmable superconducting processor. *Nature*, 574(7779):505–510, 2019.
- [2] Han-Sen Zhong, Hui Wang, Yu-Hao Deng, Ming-Cheng Chen, Li-Chao Peng, Yi-Han Luo, Jian Qin, Dian Wu, Xing Ding, Yi Hu, et al. Quantum computational advantage using photons. *Science*, 370(6523):1460–1463, 2020.
- [3] Lars S Madsen, Fabian Laudenbach, Mohsen Falamarzi Askarani, Fabien Rortais, Trevor Vincent, Jacob FF Bulmer, Filippo M Miatto, Leonhard Neuhaus, Lukas G Helt, Matthew J Collins, et al. Quantum computational advantage with a programmable photonic processor. *Nature*, 606(7912):75–81, 2022.
- [4] John Preskill. Quantum computing in the nisq era and beyond. *Quantum*, 2:79, 2018.
- [5] Kishor Bharti, Alba Cervera-Lierta, Thi Ha Kyaw, Tobias Haug, Sumner Alperin-Lea, Abhinav Anand, Matthias Degroote, Hermanni Heimonen, Jakob S Kottmann, Tim Menke, et al. Noisy intermediate-scale quantum algorithms. *Reviews of Modern Physics*, 94(1):015004, 2022.
- [6] Peter W. Shor. Polynomial-time algorithms for prime factorization and discrete logarithms on a quantum computer. *SIAM Journal on Computing*, 26(5):1484–1509, 1997.
- [7] Lov K. Grover. A fast quantum mechanical algorithm for database search. In *Proceedings of the Twenty-Eighth Annual ACM Symposium on Theory of Computing*, STOC '96, page 212–219, New York, NY, USA, 1996. Association for Computing Machinery.
- [8] M. Cerezo, Andrew Arrasmith, Ryan Babbush, Simon C. Benjamin, Suguru Endo, Keisuke Fujii, Jarrod R. McClean, Kosuke Mitarai, Xiao Yuan, Lukasz Cincio, and Patrick J. Coles. Variational quantum algorithms. *Nature Reviews Physics*, 3(9):625–644, Sep 2021.
- [9] Martin Larocca, Supanut Thanasilp, Samson Wang, Kunal Sharma, Jacob Biamonte, Patrick J. Coles, Lukasz Cincio, Jarrod R. McClean, Zoë Holmes, and M. Cerezo. A review of barren plateaus in variational quantum computing, 2024.
- [10] Antonio Sanna, Francesco Tacchino, Ivano Tavernelli, Gian Luca Giorgi, and Roberta Zambrini. Engineered dissipation to mitigate barren plateaus, 2023.
- [11] Richard P. Feynman. Simulating physics with computers. *International Journal of Theoretical Physics*, 21(6):467–488, Jun 1982.
- [12] Ehud Altman, Kenneth R. Brown, Giuseppe Carleo, Lincoln D. Carr, Eugene Demler, Cheng Chin, Brian DeMarco, Sophia E. Economou, Mark A. Eriksson, Kai-Mei C. Fu, Markus Greiner, Kaden R.A. Hazzard, Randall G. Hulet, Alicia J. Kollár, Benjamin L. Lev, Mikhail D. Lukin, Ruichao Ma, Xiao Mi, Shashank Misra, Christopher Monroe, Kater Murch, Zaira Nazario, Kang-Kuen Ni, Andrew C. Potter, Pedram Roushan, Mark Saffman, Monika Schleier-Smith, Irfan Siddiqi, Raymond Simmonds, Meenakshi Singh, I.B. Spielman, Kristan Temme, David S. Weiss, Jelena Vučković, Vladan Vuletić, Jun Ye, and Martin Zwierlein. Quantum simulators: Architectures and opportunities. *PRX Quantum*, 2:017003, Feb 2021.
- [13] Andrew J Daley, Immanuel Bloch, Christian Kokail, Stuart Flannigan, Natalie Pearson, Matthias Troyer, and Peter Zoller. Practical quantum advantage in quantum simulation. *Nature*, 607(7920):667–676, 2022.
- [14] Rahul Trivedi, Adrian Franco Rubio, and J Ignacio Cirac. Quantum advantage and stability to errors in analogue quantum simulators. *Nature Communications*, 15(1):6507, 2024.
- [15] Benedikt Fauseweh. Quantum many-body simulations on digital quantum computers: State-of-the-art and future challenges. *Nature Communications*, 15(1):2123, Mar 2024.
- [16] Yoshihisa Yamamoto and Yoshiro Takahashi. Bose-einstein condensation: A platform for quantum simulation experiments. In *Principles and Methods of Quantum Information Technologies*, pages 265–307. Springer, 2016.

- [17] Immanuel Bloch, Jean Dalibard, and Wilhelm Zwerger. Many-body physics with ultracold gases. *Rev. Mod. Phys.*, 80:885–964, Jul 2008.
- [18] N Bogoliubov. On the theory of superfluidity. *J. Phys.*, 11(1):23, 1947.
- [19] Lev Landau. The theory of superfluidity of helium ii. In *An Introduction to the Theory of Superfluidity*, pages 185–204. CRC Press, 2018.
- [20] Junheng Tao, Mingshu Zhao, and IB Spielman. Observation of anisotropic superfluid density in an artificial crystal. *Physical Review Letters*, 131(16):163401, 2023.
- [21] G Chauveau, C Maury, F Rabec, C Heintze, G Brochier, S Nascimbene, J Dalibard, J Beugnon, SM Roccuzzo, and S Stringari. Superfluid fraction in an interacting spatially modulated bose-einstein condensate. *Physical Review Letters*, 130(22):226003, 2023.
- [22] Max Heyl, Kyosuke Adachi, Yuki M Itahashi, Yuji Nakagawa, Yuichi Kasahara, Emil JW List-Kratochvil, Yusuke Kato, and Yoshihiro Iwasa. Vortex dynamics in the two-dimensional bcs-bec crossover. *Nature Communications*, 13(1):6986, 2022.
- [23] Mohit Randeria and Edward Taylor. Crossover from bardeen-cooper-schrieffer to bose-einstein condensation and the unitary fermi gas. *Annu. Rev. Condens. Matter Phys.*, 5(1):209–232, 2014.
- [24] L Barbiero, C Menotti, A Recati, and L Santos. Out-of-equilibrium states and quasi-many-body localization in polar lattice gases. *Physical Review B*, 92(18):180406, 2015.
- [25] Jun Hui See Toh, Katherine C McCormick, Xinxin Tang, Ying Su, Xi-Wang Luo, Chuanwei Zhang, and Subhadeep Gupta. Many-body dynamical delocalization in a kicked one-dimensional ultracold gas. *Nature Physics*, 18(11):1297–1301, 2022.
- [26] Anika Frölian, Craig S. Chisholm, Elettra Neri, Cesar R. Cabrera, Ramón Ramos, Alessio Celi, and Leticia Tarruell. Realizing a 1d topological gauge theory in an optically dressed bec. *Nature*, 608(7922):293–297, Aug 2022.
- [27] Sandra Buob, Jonatan Höschele, Vasilij Makhalov, Antonio Rubio-Abadal, and Leticia Tarruell. A strontium quantum-gas microscope. *PRX Quantum*, 5:020316, Apr 2024.
- [28] Christian Gross and Waseem S. Bakr. Quantum gas microscopy for single atom and spin detection. *Nature Physics*, 17(12):1316–1323, Dec 2021.
- [29] Ottó Eliasson, Jens S. Laustsen, Robert Heck, Romain Müller, Jan J. Arlt, Carrie A. Weidner, and Jacob F. Sherson. Spatial tomography of individual atoms in a quantum gas microscope. *Phys. Rev. A*, 102:053311, Nov 2020.
- [30] Stefan Kuhr. Quantum-gas microscopes: a new tool for cold-atom quantum simulators. *National Science Review*, 3(2):170–172, 04 2016.
- [31] Philipp M. Preiss, Ruichao Ma, M. Eric Tai, Jonathan Simon, and Markus Greiner. Quantum gas microscopy with spin, atom-number, and multilayer readout. *Phys. Rev. A*, 91:041602, Apr 2015.
- [32] Waseem S. Bakr, Jonathon I. Gillen, Amy Peng, Simon Fölling, and Markus Greiner. A quantum gas microscope for detecting single atoms in a hubbard-regime optical lattice. *Nature*, 462(7269):74–77, Nov 2009.
- [33] Andrew Adamatzky, Larry Bull, and B De Lacy Costello. *Unconventional computing 2007*. Luniver Press, 2007.
- [34] Danijela Marković and Julie Grollier. Quantum neuromorphic computing. *Applied physics letters*, 117(15), 2020.
- [35] Pere Mujal, Rodrigo Martínez-Peña, Johannes Nokkala, Jorge García-Beni, Gian Luca Giorgi, Miguel C Soriano, and Roberta Zambrini. Opportunities in quantum reservoir computing and extreme learning machines. *Advanced Quantum Technologies*, 4(8):2100027, 2021.
- [36] Keisuke Fujii and Kohei Nakajima. Harnessing disordered-ensemble quantum dynamics for machine learning. *Physical Review Applied*, 8(2):024030, 2017.
- [37] Gouhei Tanaka, Toshiyuki Yamane, Jean Benoit Héroux, Ryosho Nakane, Naoki Kanazawa, Seiji Takeda, Hidetoshi Numata, Daiju Nakano, and Akira Hirose. Recent advances in physical reservoir computing: A review. *Neural Networks*, 115:100–123, 2019.
- [38] Kohei Nakajima. Physical reservoir computing—an introductory perspective. *Japanese Journal of Applied Physics*, 59(6):060501, may 2020.
- [39] Kohei Nakajima and Ingo Fischer. *Reservoir computing*. Springer, 2021.
- [40] Herbert Jaeger. The “echo state” approach to analysing and training recurrent neural networks—with an erratum note. *Bonn, Germany: German National Research Center for Information Technology GMD Technical Report*, 148(34):13, 2001.
- [41] Lyudmila Grigoryeva and Juan-Pablo Ortega. Echo state networks are universal. *Neural Networks*, 108:495–508, 2018.
- [42] Antonio Sanna, Rodrigo Martínez-Peña, Miguel C Soriano, Gian Luca Giorgi, and Roberta Zambrini. Dissipation as a resource for quantum reservoir computing. *Quantum*, 8:1291, 2024.
- [43] Johannes Nokkala, Rodrigo Martínez-Peña, Gian Luca Giorgi, Valentina Parigi, Miguel C Soriano, and Roberta Zambrini. Gaussian states of continuous-variable quantum systems provide universal and versatile reservoir computing. *Communications Physics*, 4(1):53, 2021.
- [44] Rodrigo Martínez-Peña and Juan-Pablo Ortega. Quantum reservoir computing in finite dimensions. *Phys. Rev. E*, 107:035306, Mar 2023.
- [45] Pere Mujal, Johannes Nokkala, Rodrigo Martínez-Peña, Gian Luca Giorgi, Miguel C Soriano, and Roberta Zambrini. Analytical evidence of nonlinearity in qubits and continuous-variable quantum reservoir computing. *Journal of Physics: Complexity*, 2(4):045008, 2021.
- [46] L C G Govia, G J Ribeill, G E Rowlands, and T A Ohki. Nonlinear input transformations are ubiquitous in quantum reservoir computing. *Neuromorphic Computing and Engineering*, 2(1):014008, feb 2022.
- [47] Rodrigo Martínez-Peña, Gian Luca Giorgi, Johannes Nokkala, Miguel C Soriano, and Roberta Zambrini. Dynamical phase transitions in quantum reservoir computing. *Physical Review Letters*, 127(10):100502, 2021.
- [48] Rodrigo Martínez-Peña, Johannes Nokkala, Gian Luca Giorgi, Roberta Zambrini, and Miguel C Soriano. Information processing capacity of spin-based quantum reservoir computing systems. *Cognitive Computation*, pages 1–12, 2023.
- [49] Johannes Nokkala, Gian Luca Giorgi, and Roberta Zambrini. Retrieving past quantum features with deep hybrid classical-quantum reservoir computing. *arXiv preprint arXiv:2401.16961*, 2024.

- [50] Daniel Fry, Amol Deshmukh, Samuel Yen-Chi Chen, Vladimir Rastunkov, and Vanio Markov. Optimizing quantum noise-induced reservoir computing for nonlinear and chaotic time series prediction. *Scientific Reports*, 13(1):19326, 2023.
- [51] Quoc Hoan Tran and Kohei Nakajima. Higher-order quantum reservoir computing. *arXiv preprint arXiv:2006.08999*, 2020.
- [52] Wei Xia, Jie Zou, Xingze Qiu, Feng Chen, Bing Zhu, Chunhe Li, Dong-Ling Deng, and Xiaopeng Li. Configured quantum reservoir computing for multi-task machine learning. *Science Bulletin*, 68(20):2321–2329, 2023.
- [53] Laia Domingo, Mar Grande, Florentino Borondo, and Javier Borondo. Anticipating food price crises by reservoir computing. *Chaos, Solitons & Fractals*, 174:113854, 2023.
- [54] Aki Kutvonen, Keisuke Fujii, and Takahiro Sagawa. Optimizing a quantum reservoir computer for time series prediction. *Scientific reports*, 10(1):14687, 2020.
- [55] Sanjib Ghosh, Andrzej Opala, Michał Matuszewski, Tomasz Paterek, and Timothy CH Liew. Quantum reservoir processing. *npj Quantum Information*, 5(1):35, 2019.
- [56] Pere Mujal. Quantum reservoir computing for speckle disorder potentials. *Condensed Matter*, 7(1):17, 2022.
- [57] Makoto Negoro, Kosuke Mitarai, Keisuke Fujii, Kohei Nakajima, and Masahiro Kitagawa. Machine learning with controllable quantum dynamics of a nuclear spin ensemble in a solid. *arXiv:1806.10910*, 2018.
- [58] Jiayin Chen, Hendra I. Nurdin, and Naoki Yamamoto. Temporal information processing on noisy quantum computers. *Phys. Rev. Appl.*, 14:024065, Aug 2020.
- [59] Yudai Suzuki, Qi Gao, Ken C. Pradel, Kenji Yasuoka, and Naoki Yamamoto. Natural quantum reservoir computing for temporal information processing. *Scientific Reports*, 12(1):1353, Jan 2022.
- [60] Tomoyuki Kubota, Yudai Suzuki, Shumpei Kobayashi, Quoc Hoan Tran, Naoki Yamamoto, and Kohei Nakajima. Temporal information processing induced by quantum noise. *Phys. Rev. Res.*, 5:023057, Apr 2023.
- [61] Toshiki Yasuda, Yudai Suzuki, Tomoyuki Kubota, Kohei Nakajima, Qi Gao, Wenlong Zhang, Satoshi Shimono, Hendra I Nurdin, and Naoki Yamamoto. Quantum reservoir computing with repeated measurements on superconducting devices. *arXiv preprint arXiv:2310.06706*, 2023.
- [62] Alen Senanian, Sridhar Prabhu, Vladimir Kremenetski, Saswata Roy, Yingkang Cao, Jeremy Kline, Tatsuhiko Onodera, Logan G Wright, Xiaodi Wu, Valla Fatemi, et al. Microwave signal processing using an analog quantum reservoir computer. *Nature Communications*, 15(1):7490, 2024.
- [63] Alessia Suprano, Danilo Zia, Luca Innocenti, Salvatore Lorenzo, Valeria Cimini, Taira Giordani, Ivan Palmisano, Emanuele Polino, Nicolò Spagnolo, Fabio Sciarino, G. Massimo Palma, Alessandro Ferraro, and Mauro Paternostro. Experimental property reconstruction in a photonic quantum extreme learning machine. *Phys. Rev. Lett.*, 132:160802, Apr 2024.
- [64] Rodrigo Araiza Bravo, Khadijeh Najafi, Xun Gao, and Susanne F. Yelin. Quantum reservoir computing using arrays of rydberg atoms. *PRX Quantum*, 3:030325, Aug 2022.
- [65] Milan Kornjača, Hong-Ye Hu, Chen Zhao, Jonathan Wurtz, Phillip Weinberg, Majd Hamdan, Andrii Zhdanov, Sergio H. Cantu, Hengyun Zhou, Rodrigo Araiza Bravo, Kevin Bagnall, James I. Basham, Joseph Campo, Adam Choukri, Robert DeAngelo, Paige Frederick, David Haines, Julian Hammett, Ning Hsu, Ming-Guang Hu, Florian Huber, Paul Niklas Jepsen, Ningyuan Jia, Thomas Karolyshyn, Minhho Kwon, John Long, Jonathan Lopatin, Alexander Lukin, Tommaso Macrì, Ognjen Marković, Luis A. Martínez-Martínez, Xianmei Meng, Evgeny Ostroumov, David Paquette, John Robinson, Pedro Sales Rodriguez, Anshuman Singh, Nandan Sinha, Henry Thoreen, Noel Wan, Daniel Waxman-Lenz, Tak Wong, Kai-Hsin Wu, Pedro L. S. Lopes, Yuval Boger, Nathan Gemelke, Takuya Kitagawa, Alexander Keesling, Xun Gao, Alexei Bylinskii, Susanne F. Yelin, Fangli Liu, and Sheng-Tao Wang. Large-scale quantum reservoir learning with an analog quantum computer. *arXiv*, arXiv:2407.02553, 2024.
- [66] Matthew P. A. Fisher, Peter B. Weichman, G. Grinstein, and Daniel S. Fisher. Boson localization and the superfluid-insulator transition. *Phys. Rev. B*, 40:546–570, Jul 1989.
- [67] Markus Greiner, Olaf Mandel, Tilman Esslinger, Theodor W. Hänsch, and Immanuel Bloch. Quantum phase transition from a superfluid to a mott insulator in a gas of ultracold atoms. *Nature*, 415(6867):39–44, Jan 2002.
- [68] W. S. Bakr, A. Peng, M. E. Tai, R. Ma, J. Simon, J. I. Gillen, S. Fölling, L. Pollet, and M. Greiner. Probing the superfluid-to-mott insulator transition at the single-atom level. *Science*, 329(5991):547–550, 2010.
- [69] Jacob F. Sherson, Christof Weitenberg, Manuel Endres, Marc Cheneau, Immanuel Bloch, and Stefan Kuhr. Single-atom-resolved fluorescence imaging of an atomic mott insulator. *Nature*, 467(7311):68–72, Sep 2010.
- [70] Takafumi Tomita, Shuta Nakajima, Ipei Danshita, Yosuke Takasu, and Yoshiro Takahashi. Observation of the mott insulator to superfluid crossover of a driven-dissipative bose-hubbard system. *Science Advances*, 3(12), December 2017.
- [71] Lukas Pausch, Edoardo G Carnio, Alberto Rodríguez, and Andreas Buchleitner. Chaos and ergodicity across the energy spectrum of interacting bosons. *Physical Review Letters*, 126(15):150601, 2021.
- [72] Lukas Pausch, Edoardo G Carnio, Andreas Buchleitner, and Alberto Rodríguez. Chaos in the bose-hubbard model and random two-body hamiltonians. *New Journal of Physics*, 23(12):123036, dec 2021.
- [73] Matthew Dale, Simon O’Keefe, Angelika Sebald, Susan Stepney, and Martin A Trefzer. Reservoir computing quality: connectivity and topology. *Natural Computing*, 20:205–216, 2021.
- [74] JB Mallinson, ZE Heywood, RK Daniels, MD Arnold, PJ Bones, and SA Brown. Reservoir computing using networks of memristors: effects of topology and heterogeneity. *Nanoscale*, 15(22):9663–9674, 2023.
- [75] Aaron Griffith, Andrew Pomerance, and Daniel J Gauthier. Forecasting chaotic systems with very low connectivity reservoir computers. *Chaos: An Interdisciplinary Journal of Nonlinear Science*, 29(12), 2019.
- [76] Wendson AS Barbosa, Aaron Griffith, Graham E Rowlands, Luke CG Govia, Guilhem J Ribeill, Minh-Hai Nguyen, Thomas A Ohki, and Daniel J Gauthier.

- Symmetry-aware reservoir computing. *Physical Review E*, 104(4):045307, 2021.
- [77] Joschka Herteux and Christoph R ath. Breaking symmetries of the reservoir equations in echo state networks. *Chaos: An Interdisciplinary Journal of Nonlinear Science*, 30(12), 2020.
- [78] Andrew Flynn, Joschka Herteux, Vassilios A Tsachouridis, Christoph R ath, and Andreas Amann. Symmetry kills the square in a multifunctional reservoir computer. *Chaos: An Interdisciplinary Journal of Nonlinear Science*, 31(7), 2021.
- [79] Till D K uhner, Steven R White, and Hartmut Monien. One-dimensional bose-hubbard model with nearest-neighbor interaction. *Physical Review B*, 61(18):12474, 2000.
- [80] S Ejima, H Fehske, and F Gebhard. Dynamic properties of the one-dimensional bose-hubbard model. *Europhysics Letters*, 93(3):30002, 2011.
- [81] Thilo St oferle, Henning Moritz, Christian Schori, Michael K ohl, and Tilman Esslinger. Transition from a strongly interacting 1d superfluid to a mott insulator. *Phys. Rev. Lett.*, 92:130403, Mar 2004.
- [82] I. B. Spielman, W. D. Phillips, and J. V. Porto. Mott-insulator transition in a two-dimensional atomic bose gas. *Phys. Rev. Lett.*, 98:080404, Feb 2007.
- [83] M. K ohl, H. Moritz, T. St oferle, C. Schori, and T. Esslinger. Superfluid to mott insulator transition in one, two, and three dimensions. *Journal of Low Temperature Physics*, 138(3):635–644, Feb 2005.
- [84] Andrey R Kolovsky and Andreas Buchleitner. Quantum chaos in the bose-hubbard model. *Europhysics Letters*, 68(5):632, 2004.
- [85] Vadim Oganesyan and David A Huse. Localization of interacting fermions at high temperature. *Physical review b*, 75(15):155111, 2007.
- [86] H. A. Weidenm uller and G. E. Mitchell. Random matrices and chaos in nuclear physics: Nuclear structure. *Rev. Mod. Phys.*, 81:539–589, May 2009.
- [87] Luca D’Alessio, Yariv Kafri, Anatoli Polkovnikov, and Marcos Rigol. From quantum chaos and eigenstate thermalization to statistical mechanics and thermodynamics. *Advances in Physics*, 65(3):239–362, 2016.
- [88] Yasar Y Atas, Eugene Bogomolny, Olivier Giraud, and Guillaume Roux. Distribution of the ratio of consecutive level spacings in random matrix ensembles. *Physical review letters*, 110(8):084101, 2013.
- [89] Olivier Giraud, Nicolas Mac e, Eric Vernier, and Fabien Alet. Probing symmetries of quantum many-body systems through gap ratio statistics. *Physical Review X*, 12(1):011006, 2022.
- [90] Ana Palacios, Rodrigo Mart inez-Pe na, Miguel C Soriano, Gian Luca Giorgi, and Roberta Zambrini. Role of coherence in many-body quantum reservoir computing. *arXiv preprint arXiv:2409.17734*, 2024.
- [91] Jakob Lindinger, Andreas Buchleitner, and Alberto Rodr iguez. Many-body multifractality throughout bosonic superfluid and mott insulator phases. *Physical review letters*, 122(10):106603, 2019.
- [92] Guillem Llodr a, Christos Charalambous, Gian Luca Giorgi, and Roberta Zambrini. Benchmarking the role of particle statistics in quantum reservoir computing. *Advanced Quantum Technologies*, 6(1):2200100, 2023.
- [93] Arthur E Hoerl and Robert W Kennard. Ridge regression: applications to nonorthogonal problems. *Technometrics*, 12(1):69–82, 1970.
- [94] James Vere Beck and Kenneth J Arnold. *Parameter estimation in engineering and science*. James Beck, 1977.
- [95] Pere Mujal, Rodrigo Mart inez-Pe na, Gian Luca Giorgi, Miguel C Soriano, and Roberta Zambrini. Time-series quantum reservoir computing with weak and projective measurements. *npj Quantum Information*, 9(1):16, 2023.
- [96] Fangjun Hu, Gerasimos Angelatos, Saeed A Khan, Marti Vives, Esin T ureci, Leon Bello, Graham E Rowlands, Guilhem J Ribeill, and Hakan E T ureci. Tackling sampling noise in physical systems for machine learning applications: Fundamental limits and eigentasks. *Physical Review X*, 13(4):041020, 2023.
- [97] Jorge Garc a-Beni, Gian Luca Giorgi, Miguel C Soriano, and Roberta Zambrini. Scalable photonic platform for real-time quantum reservoir computing. *Physical Review Applied*, 20(1):014051, 2023.
- [98] Julien Dudas, Baptiste Carles, Erwan Plouet, Frank Alice Mizrahi, Julie Grollier, and Danijela Markovi c. Quantum reservoir computing implementation on coherently coupled quantum oscillators. *npj Quantum Information*, 9(1):64, 2023.
- [99] WD Kalfus, GJ Ribeill, GE Rowlands, HK Krovi, TA Ohki, and LCG Govia. Hilbert space as a computational resource in reservoir computing. *Physical Review Research*, 4(3):033007, 2022.
- [100] Paolo Stornati, Antonio Acin, Ulysse Chabaud, Alexandre Dauphin, Valentina Parigi, and Federico Cennone. Variational quantum simulation using non-gaussian continuous-variable systems. *arXiv preprint arXiv:2310.15919*, 2023.
- [101] Wei Xia, Jie Zou, Xingze Qiu, and Xiaopeng Li. The reservoir learning power across quantum many-body localization transition. *Frontiers of Physics*, 17(3):33506, 2022.
- [102] Joni Dambre, David Verstraeten, Benjamin Schrauwen, and Serge Massar. Information processing capacity of dynamical systems. *Scientific reports*, 2(1):514, 2012.
- [103] Amir F Atiya and Alexander G Parlos. New results on recurrent network training: unifying the algorithms and accelerating convergence. *IEEE transactions on neural networks*, 11(3):697–709, 2000.
- [104] F. Mattiotti, J. Dubail, D. Hagenm uller, J. Schachenmayer, J.-P. Brantut, and G. Pupillo. Multifractality in the interacting disordered tavis-cummings model. *Phys. Rev. B*, 109:064202, Feb 2024.